



ELSEVIER



CrossMark

Available online at www.sciencedirect.com

ScienceDirect

Proceedings of the Combustion Institute 35 (2015) 1409–1416

Proceedings
of the
Combustion
Institute

www.elsevier.com/locate/proci

Simultaneous multi-species and temperature visualization of premixed flames in the distributed reaction zone regime

Bo Zhou^a, Christian Brackmann^a, Zhongshan Li^{a,*}, Marcus Aldén^a,
Xue-Song Bai^b

^a Division of Combustion Physics, Lund University, P.O. Box 118, S-221 00 Lund, Sweden

^b Division of Fluid Mechanics, Lund University, P.O. Box 118, S-221 00 Lund, Sweden

Available online 19 July 2014

Abstract

Structures of turbulent premixed flames, operating in the thin and distributed reaction zone regimes, were investigated for stoichiometric premixed methane/air jet flames with jet Reynolds number up to 40,000 and corresponding Karlovitz number up to 286. Multi-species planar laser-induced fluorescence with high spatial resolution was applied to simultaneously image combinations of CH/OH/CH₂O and HCO/OH/CH₂O. In addition, OH/CH₂O imaging was performed in combination with simultaneous Rayleigh scattering thermometry. The CH and HCO layers showed progressive broadening along the axial distance for flames with Reynolds number above 21,000 and the corresponding Karlovitz number above 126. At Reynolds number 40,000 and the corresponding Karlovitz number of 286, a mean CH layer thickness more than 10 times larger than that under laminar condition was observed, providing a clear experimental evidence of distributed reaction zone owing to turbulence/flame interaction. Additionally, spatial correlations between species show that OH and CH₂O locate at mutually exclusive regions. In contrast, both CH and HCO can overlap substantially with CH₂O. The regions of strong CH/HCO signals correspond to regions with weak CH₂O signals. Moreover, CH and HCO are shown to be able to penetrate deeper into the OH layer than CH₂O. Regions where CH and HCO appear distributed show a rather homogeneous temperature distribution with reduced maximum temperature compared with non-distributed conditions. © 2014 The Combustion Institute. Published by Elsevier Inc. All rights reserved.

Keywords: Planar laser-induced fluorescence; Distributed reaction zone; CH and HCO radicals; Turbulent combustion; Premixed methane/air flame

1. Introduction

Modeling and understanding of high-intensity and small-scale turbulent premixed combustion

remain a scientific challenge. Turbulent premixed combustion has been theoretically categorized into regimes depending on the interactions between turbulence and chemistry. For low-intensity and large-scale turbulent flames, the laminar flamelet concept [1] is widely adopted in numerical simulations based on the assumption that the

* Corresponding author. Fax: +46 46 222 4542.

E-mail address: Zhongshan.li@forbrf.lth.se (Z. Li).

smallest scale of turbulence, the Kolmogorov scale, is larger than the length scale of the reaction zones. The flamelet concept has been verified in the wrinkled/corrugated flamelet regimes by many experiments and direct numerical simulations (DNS) [2–4]. Peters [5] described the turbulence/flame interaction in the thin-reaction-zone (TRZ) regime where small eddies are sufficiently small to fit into the preheat zone but still comparatively larger than the reaction zone thickness, thus broadening the preheat zone while the thin reaction zone remains intact. This regime has also been verified in numerical simulations and experiments [6–11].

When the Kolmogorov scale becomes an order of magnitude smaller than the flame thickness (i.e. Karlovitz number, $Ka > 100$), the flame is in the so-called distributed reaction zone (DRZ) regime. In the DRZ regime it is theoretically expected that the smallest eddies can penetrate into the thin reaction zone, and thereby broaden the reaction zone through turbulence-enhanced diffusive transfer of heat and species. In contrast, Poludnenko et al. [12] showed a DNS simulation of methane/air flames, which implies that the flamelet concept could still be valid even in the DRZ regime. However, the single-step chemistry assumed in their simulation could be questionable in the DRZ regime where finite-rate chemistry effects interacting with turbulence are expected to be important. It has also been argued that the DRZ regime may not be realized in practice because the flame front might incline to extinction before being broadened, as evidenced in observations of Meier et al. [13] and Chen et al. [7]. Thus, up to now it seems that no consistent physical understanding of turbulence/chemistry interaction in the DRZ regime has been established, a fact many times leading to the arbitrary assumption that the flamelet concept is always applicable.

It is of particular importance to investigate turbulent combustion in this regime for some practical applications, e.g., stationary gas turbines for power generation [14]. However, numerical and experimental investigations in the DRZ regime are rather limited. Some reported observations of vitiated thermal gradients at highly turbulent conditions might imply the existence of distributed reactions [15]. Nevertheless, a direct measure of radicals such as CH and HCO that only exist in a thin reaction zone, from the flamelet perspective, can be much more convincing. As proposed by Driscoll, “a documented distributed reaction zone is defined as a set of measured images of the heat release region or images of radicals such as CH that are spread out over distances that are many times larger than the thickness of a laminar flame” [16]. To the best of authors’ knowledge, no such persuasive proof that distributed reactions can be generated through turbulence has been reported.

The aim of this work is to gain deepened physical and phenomenological understandings of turbulence/chemistry interaction in the DRZ regime with special emphasis on investigating the feasibility of flame front thickening by turbulence. It has been demonstrated that simultaneous multi-species planar laser-induced fluorescence (PLIF) visualization bears great merits for characterizing turbulent flame structures [17]. Improved PLIF diagnostics of CH [18] and HCO [19] developed recently in our lab provide powerful tools for flame reaction zone characterization. In this work, a series of premixed methane/air flames at conditions with various flow speeds were investigated covering both the TRZ and DRZ regimes. Simultaneous PLIF measurements of CH_2O (typical preheat zone marker) and OH (typical oxidation and post-flame zone marker) were performed synchronously with (a) CH PLIF, (b) HCO PLIF, and (c) Rayleigh scattering temperature measurements in turn.

2. Experimental setup

A hybrid porous-plug/jet burner was employed, consisting of a porous bronze plug (61 mm in diameter) and a central jet. The exit of the central jet is located 2 mm above the porous-plug burner surface, and the outer and inner diameters of the jet are 7 and 1.5 mm, respectively. Figure 1a shows a photograph of a turbulent jet methane/air flame and a schematic of the burner. A laminar methane/air co-flow flame (0.3 m/s, $\Phi = 0.9$) was established on the porous-plug burner, while stoichiometric methane/air jet flames were operated at various flow speeds (v_0) as summarized in Table 1. The flow speeds controlled by mass flow controllers (Bronkhorst) were calibrated at 300 K, giving an uncertainty of 1%. The lean co-flow flame provides a hot environment, sustaining the jet flame through continuous ignition of the fuel/air mixture from the central jet, and preventing the entrainment of ambient cold air into the jet flame. The burner is similar to burners studied in several other groups [7,20,21], where the velocity field was measured at various jet velocities. Based on laminar burning velocity (S_L) data reported in [21], flame structure analysis [22], and Peters formulation of the Karlovitz number (Ka) and turbulent Reynolds number (Re_t) [5], an estimation of the Ka and Re_t has been carried out for the flames studied in this work. The value of Ka is presented in Table 1, which ranges from 10 and 286, covering the TRZ regime (F1, F2) and the DRZ regime (F3–F5). The velocity of turbulent eddies at the integral scale (v') is estimated from the root-mean-square velocity data of Dunn et al. [21] at the height above the burner (HAB) about 30 jet diameters. The integral length (l_0) is estimated as the full width at half maximum of

Table 1
Flame conditions.

| Flame | ϕ | v_0 (m/s) | v'/S_L | Ka | Re_{jet} | Re_l | l_0 (mm) |
|-------|--------|-------------|----------|------|------------|--------|------------|
| F0 | 1.0 | 11 | — | — | 1050 | — | — |
| F1 | 1.0 | 66 | 8 | 10 | 6300 | 51 | 2.1 |
| F2 | 1.0 | 110 | 28 | 49 | 10,500 | 257 | 3.2 |
| F3 | 1.0 | 220 | 56 | 126 | 21,000 | 625 | 3.9 |
| F4 | 1.0 | 330 | 84 | 202 | 31,500 | 1227 | 5.1 |
| F5 | 1.0 | 418 | 107 | 286 | 40,000 | 1584 | 5.2 |

the measured profile of mean CH_2O layer, because CH_2O exists in the low temperature preheat zone [11], and in turbulent flames it is transported by turbulence eddies to the low temperature unburned side of the flame. The thickness of the mixing layer increases with the height above the burner; the integral length shown in Table 1 is the value at HAB of 45 mm (30 jet diameters), which is consistent with the selection of the velocity of turbulent eddies at the integral scale from the experiments. Based on the integral length scale the turbulent Reynolds number (Re_t) is estimated to range from 51 (F1) to 1548 (F6), and the Kolmogorov scale from 110 μm (F1) to 21 μm (F6).

A schematic of the experimental setup is shown in Fig. 1b. A Nd:YAG laser (Quanta-Ray-PRO-250-10, Spectra Physics) was used to pump a dye-laser (Cobra Stretch-G-2400, Sirah) operated with dye Rhodamine 590, delivering radiation at 283 nm, which was fine tuned to the $Q_1(8)$ transition in the $\text{A}^2\Sigma^+-\text{X}^2\Pi$ (1-0) band for OH excitation. A third harmonic 355-nm beam generated from the same Nd:YAG laser was used to probe CH_2O [23]. These two laser beams are spatially combined through a dichroic mirror prior to the sheet-forming optics. Excitation of CH at 387 nm and HCO at 259 nm, employing a separate alexandrite laser (101PAL, Light Age), were adopted following the excitation–detection

schemes developed in our previous works [18,19]. Potential interferences to PLIF detection of HCO [19] and CH [18] have previously been rigorously investigated including the flame conditions applied in the present work. For HCO PLIF, same optical system was utilized to guaranty interference-free measurements. For CH PLIF, since the previous work [18] was performed using an alexandrite laser of different type, CH LIF emission spectra have been carefully examined and no detectable spectral interference signal has been found. All the laser pulses were synchronized and a 200 ns delay was applied to the alexandrite laser to avoid signal crosstalk. The alexandrite laser beam was aligned with the 283-nm/355-nm beams using a prism but shifted vertically around 2 mm. The main part of the three laser sheets became spatially overlapped after passing through the same sheet-forming optics which comprised a cylindrical lens ($f = -40$ mm) and a spherical lens ($f = 200$ mm). The spatially overlapped region of laser sheets with relatively uniform intensity distributions was selected by employing a 22-mm aperture. To achieve proper focusing of all laser sheets just above the center of the jet, two telescope systems were inserted into the optical paths of the 283 nm and 355 nm laser beams to slightly adjust beam divergence. The thickness of all laser sheets around 100 μm over the measurement region was

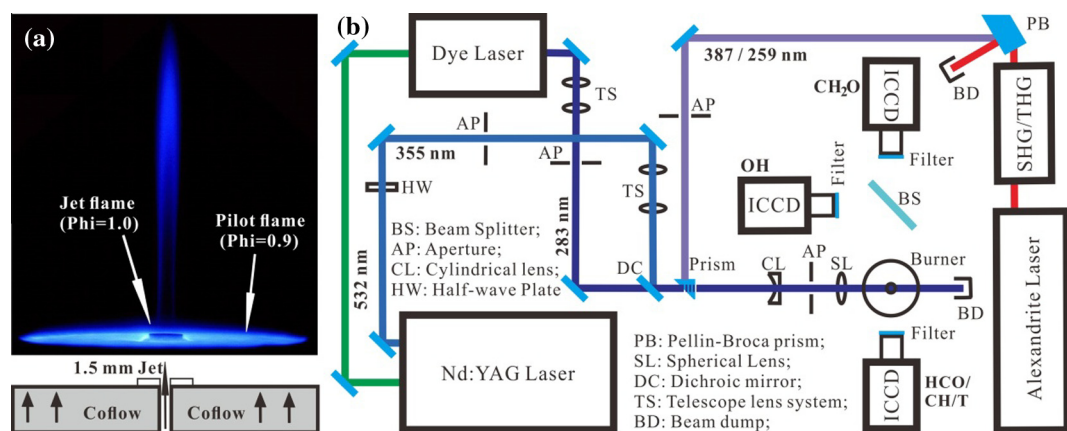


Fig. 1. (a) Photograph of a turbulent methane/air jet flame with a schematic of the porous-plug/jet burner. (b) Schematic of experimental setup for multi-species PLIF and Rayleigh scattering.

estimated from burned marks of all laser sheets on photo-sensitive paper. The 355 nm laser employed for CH₂O excitation was also used for planar Rayleigh scattering thermometry with a half-wave plate additionally inserted into the beam to achieve vertical polarization for maximum Rayleigh signal.

The detection system included three intensified CCD cameras arranged as depicted in Fig. 1b. A beam splitter ($R > 99.9\%$ @ 287–355 nm and $T > 90\%$ @ 400–700 nm) was used to separate OH- and CH₂O-signals detected by two cameras (512 × 512 pixels, PI-MAX I, Princeton Instruments). A camera (1024 × 1024 pixels PI-MAX III, Princeton Instruments) positioned opposite to the CH₂O camera was employed for CH, HCO or temperature measurements. All PLIF and temperature images were spatially correlated pixel-by-pixel through imaging the same grid target with each camera. The spatial resolution of each camera was determined by imaging a resolution target (USAF-1951) and analysis the finest resolvable pattern. Further experimental details are summarized in Table 2 together with estimated signal-to-noise ratios (SNR) based on the ratio between signal mean value and standard deviation on the region absent of signal. It should be noted that the noise was estimated from non-signal regime, which might lead to slight overestimation of SNR values summarized in Table 2.

3. Results and discussion

In the following, results from three series of simultaneous measurements are presented: (1) CH/CH₂O/OH, (2) HCO/CH₂O/OH and (3) T/CH₂O/OH. Each series consists of 500 single-shot images for each signal. All images have been flat-field corrected and processed by a 2 × 2 pixels median filter to reduce noise. The imaging resolution of 50–70 μm remains as confirmed by processing the fine flame structures in PLIF images (c.f. Fig. 2(A4–C4)). This resolution gives 40–60 points for resolving the integral turbulence eddies and the associated broadening of the reaction

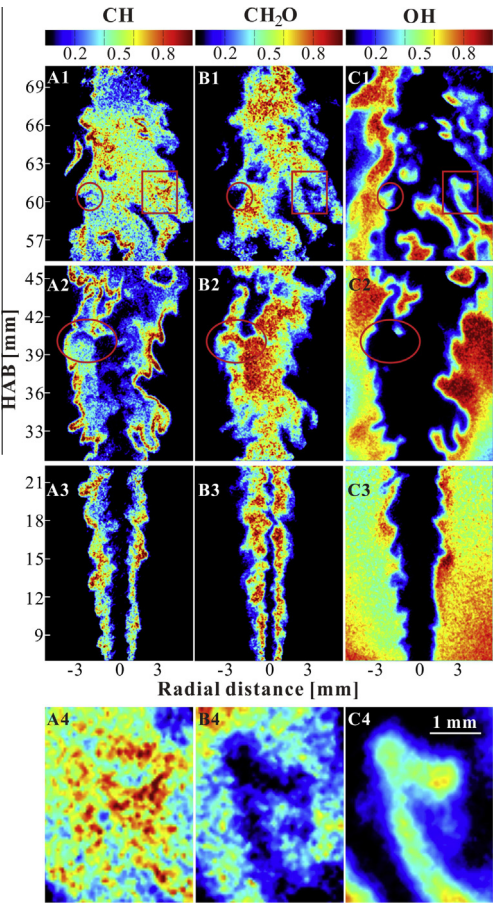


Fig. 2. Simultaneous CH/CH₂O/OH PLIF images measured in flame F5 at HABs 63, 39 and 15 mm. The last row shows local detail structures of the regions marked by the rectangles.

zones. It is also fine enough to resolve the Kolmogorov eddies in F1 and F2 flames, but slightly coarser than the Kolmogorov scales in F3–F5 flames. Intensities of PLIF images were displayed in grayscale (from 0 to 1), and the strongest signal up to 1% of total signal pixels were set

Table 2
Experimental parameters and signal-to-noise ratio for the laser-based measurements.

| Species | CH | HCO | T | OH | CH ₂ O |
|---------------------------------------|-----------------------------|-----------------------|-----------------------|-------------------------|-----------------------------|
| Objectives (mm) | $f_{\#} = 1.2,$ $f = 50$ | $f_{\#} = 2, f = 100$ | $f_{\#} = 2, f = 100$ | $f_{\#} = 2.5, f = 150$ | $f_{\#} = 1.4,$ $f = 85$ |
| Spatial resolution (μm ³) | 70 ² × 00 | 56 ² × 100 | 56 ² × 100 | 70 ² × 100 | 70 ² × 100 |
| Pulse energy (mJ) | 70 | 26 | 120 | 10 | 120 |
| Pulse length (ns) | 50 | 50 | 8 | 8 | 8 |
| Optical filter | GG400 | Longpass | Bandpass | Bandpass | GG400 |
| | | 266 nm | 355 ± 5 nm | 325 ± 25 nm | |
| Linewidth (cm ⁻¹) | 2 | 2.4 | 2 | 0.3 | 2 |
| SNR | >17 | >8 | >10 | >32 | >28 |

to 1. More examples for each series of flame F5 are included in [Supplement](#).

3.1. Structures of CH/CH₂O/OH layers

As a short-lived intermediate radical, CH has been recognized as a typical flame front marker [24] and CH PLIF has been utilized as a diagnostic tool for turbulent combustion [25,26]. An example of simultaneous CH/CH₂O/OH PLIF measurements is shown in [Fig. 2](#), for flame F5 ($Ka = 286$, thus a flame in the DRZ regime) at three flame heights (about 15, 39 and 63 mm above burner). The velocity measurements reported in [21,22] indicated that at high Reynolds numbers the turbulence intensity increases with the distance to the burner up to $x/D = 20$ –30, where x is the height above the burner, HAB, and D is the inner diameter of the jet. Thereafter, the turbulence intensity decreases due to dissipation of turbulence kinetic energy. Accordingly, in the present flames (F3–F5) maximum turbulence is expected to be around 30–45 mm, i.e. [Fig. 2\(A2–C2\)](#). The CH₂O layer in flame F5 is clearly broadened by the intensive turbulence eddies and the thickness increases with HAB and turbulence intensity. At the peak turbulence intensity, [Fig. 2\(B2\)](#), CH₂O is shown to occupy the entire inner region of the flame, and the CH₂O and OH layers appear mutually exclusive in space. At the top and middle measurement positions, some isolated patchy OH regions can be found, similar to the observation of Dunn et al. [21] for flames in the DRZ regime.

Similar to the CH₂O distribution, the CH layer shows progressive broadening with HAB, [Fig. 2\(A1–A3\)](#). At low HAB, [Fig. 2\(A3\)](#), the CH layer is not substantially broader than the thickness of the CH layer in the corresponding laminar flame. As turbulence develops along the axial direction (cf. [Fig. 2\(A2\)](#)), the CH layers start to penetrate towards the CH₂O side, while sharp CH gradients still remain at the interfaces between CH and OH regions. As highlighted by the circle in [Fig. 2\(A2–C2\)](#), CH can coexist with CH₂O in space, where low CH₂O signal correlates with strong CH signal and vice versa. At the top position, [Fig. 2\(A1\)](#), CH spreads over the entire domain enclosed by OH, and the CH distribution can completely overlap with and even become wider than the CH₂O region. Slight inhomogeneity of CH signals is seen to mostly correspond to the interface where CH and OH have interacted or are overlapped. A closer comparison of spatial correlations between CH and OH distributions indicates that CH penetrates into the OH region, deeper than CH₂O, and coexists with OH in regions of moderate OH signal, c.f. regions highlighted by the circles and rectangles in [Fig. 2\(A1–C1\)](#). The regions marked by the rectangles are displayed in the last row of [Fig. 2](#). The

spatial correlations between CH, CH₂O and OH with local detail structures down to the resolution limit ($\sim 60 \mu\text{m}$) can still be identified.

Driscoll [16] indicated that a measured flamelet could be a few (3–4) times thicker than an unstrained laminar flame due to (1) limited experimental spatial resolution, (2) three-dimensional effects in PLIF measurements, and (3) applied strain rate. In present work, spatial resolution given by the $100 \mu\text{m}$ laser sheet and the imaging resolutions of 50 – $70 \mu\text{m}$ is sufficient to resolve structures of thin laminar flames and determine the flame front thickness [16]. The observed CH broadening up to a few millimeters as shown in [Fig. 2\(A1\)](#) cannot be explained by three-dimensional effects or strain rate. Therefore, the observed thickening of the CH layer is attributed to the rapid transport by the small-scale turbulence eddies of rather short turnover time, comparable to the chemical reaction time involving CH.

3.2. Structures of HCO/CH₂O/OH layers

The HCO radical has since long been recognized as one of the most important intermediate species and a marker of major heat release in hydrocarbon combustion [24,27]. Since single-shot HCO PLIF was not previously feasible due to low signal levels, the product of simultaneously imaged OH and CH₂O distributions was pro-

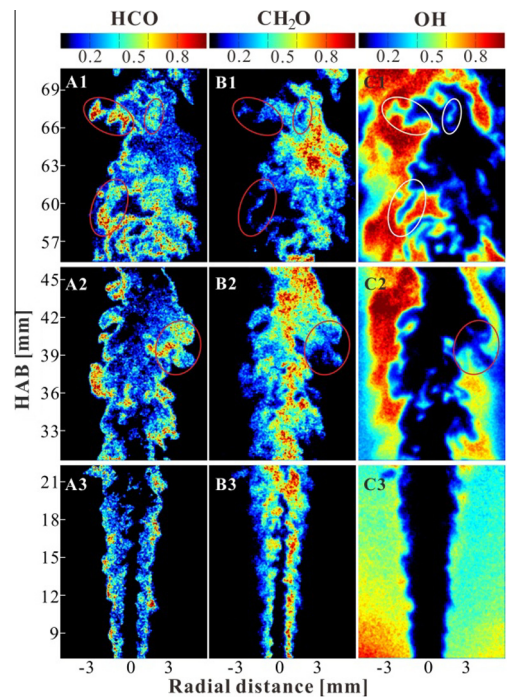


Fig. 3. Simultaneous HCO/CH₂O/OH PLIF images measured in flame F5 at HABs 63, 39 and 15 mm.

posed as a quantity for indirect measurement of HCO and heat release [24] being utilized in studies of turbulent combustion [28]. Recently the feasibility of single-shot interference-free PLIF HCO imaging in turbulent flames has been demonstrated [19]. To the best of authors' knowledge, the present work demonstrates the first multi-species PLIF imaging that includes the HCO radical.

A set of HCO/CH₂O/OH PLIF images for flame F5 is shown in Fig. 3. Similar observations comparing with the CH/CH₂O/OH series in Fig. 2 can be made and summarized as follows: (a) the HCO regions also show progressive broadening with increasing HAB; (b) HCO can spatially overlap with CH₂O and regions of strong HCO signals correlate with relatively weak CH₂O signals and vice versa; (c) HCO can penetrate deeper into the OH region than CH₂O and overlap with OH regions of moderate or high signal, as highlighted by the circles in Fig. 3(A1–C1) and (A2–C2). Additionally, HCO appears to be slightly sharper than CH at the edges where HCO and OH interact.

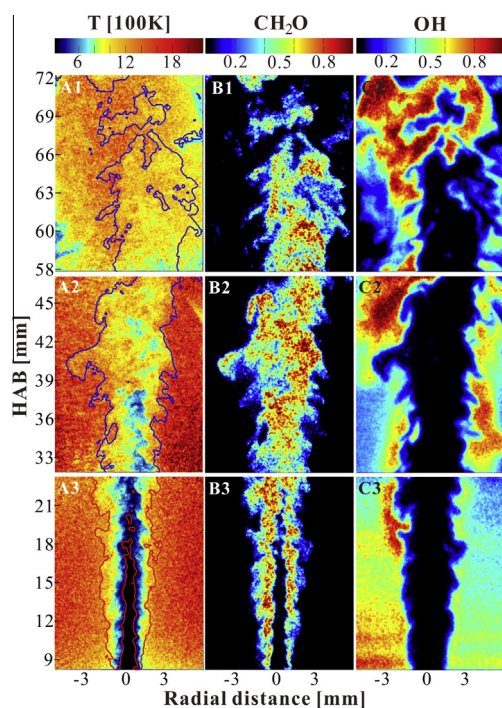


Fig. 4. Simultaneous T/CH₂O/OH measurements in flame F5 at HABs 63, 39 and 15 mm. Iso-intensity contours of 10% maximum CH₂O intensities were superimposed on temperature fields for comparison. A homogenous temperature distribution is approached with increasing HAB.

3.3. Temperature fields and structures of CH₂O/OH layers

Rayleigh scattering has been performed simultaneously with CH₂O and OH PLIF to monitor the temperature distribution of flames, for which distributed CH and HCO have been observed. The Rayleigh signals were evaluated using cross section data from ref. [29]. An example of temperature, CH₂O and OH measurements for flame F5 is shown in Fig. 4. Contours of CH₂O (iso-intensity lines at 10% of the maximum signal) were superimposed on the temperature field for comparison. At low HAB, Fig. 4(A3), a sharp thermal gradient across the flame can be identified, owing to the locally low turbulence intensity. While OH exists in high temperature regions (mostly above 1500 K), a temperature range from approximately 400 to 900 K can be assigned to the broadened CH₂O layer (red curve). Further downstream, Fig. 4(A2), turbulence develops to higher intensity, resulting in a broader preheat zone along with broader distributions of CH₂O, CH, and HCO. As a consequence, the thermal thickness of the flame, defined as the distance between two isothermal contours, becomes larger. This is consistent with reported observations that turbulence can increase the temperature in the preheat zone [30,31]. At the top measurement position, the overall temperature field appears more homogeneous, although OH-regions show slightly higher (~200 K) temperature. Additionally, the maximum temperature was reduced from ~1900 K, cf. Fig. 4(A2) and (A3), to ~1500 K, cf. Fig. 4(A1), through mixing with ambient cold air. Entrainment from ambient cold air can also be seen from low temperature regions on the edges of Fig. 4(A1).

Comparing the temperature field with other compositional fields (cf. Figs. 2–4), it can be seen that high-intensity OH regions mostly correlate with high-temperature regions where oxidizations of species, such as CH, HCO and CH₂O, proceed rapidly. This explains the observation of mutually exclusive distributions of OH and CH₂O [11]. Conversely, with relatively lower temperature and much less OH in the CH₂O regions, e.g. at the top position of flame F5, the oxidation process becomes slower. Therefore, the CH and HCO layers enclosed by OH appear more distributed. These observations from both temperature and compositional fields support the hypothesis of a distributed reaction zone where flame propagation is eliminated by rapid turbulent mixing so that no distinct localized temperature gradient can be observed. A homogeneous temperature distribution with reduced maximum temperature, as observed in Fig. 4(A1), has also been used to characterize the concepts of flameless oxidation [32] and mild combustion [33,34].

Even though the CH and HCO PLIF measurements are not quantitative, the CH and HCO LIF signals can be considered to give a reasonably good qualitative representation of the concentration variations in the reacting flow for the temperature range (~ 1200 – 1600 K) of the middle and top positions. Information on temperature dependence of CH and HCO LIF signals can be found in Ref. [18,27].

3.4. CH-layer thickness

To examine the flame structures at different turbulence intensities, ensemble averaged mean CH layer thickness (based on 250 samples) at different HABs was evaluated for different jet speeds. The thickness was defined as the integrated area under a signal intensity profile normalized by the maximum value. This definition gives a reasonable measure of CH layer thickness ($327\text{ }\mu\text{m}$) for the laminar flame F0 as compared with an analysis of full-width at half maximum ($315\text{ }\mu\text{m}$). The thickness was calculated from profiles along the horizontal (radial) direction at selected HAB positions. In addition, a thickness was evaluated from vertical (axial) intensity profiles at the position where the horizontal profile intersects with the CH layer, in order to account for the wrinkled flame front that sometimes has horizontal orientations in the image. The minimum evaluated value was selected to represent the CH layer thickness. Through this approach, the measured CH thickness was considered to be overestimated due to flame front orientations at varying angle by at most 50%. When distributed CH was approached, and thus no distinct flame front can be identified (i.e. at top measurement position of flames F4 and F5), only horizontal CH layer thickness was calculated. In Fig. 5, the measured CH thickness (δ_T) normalized by the CH thickness (δ_0) measured in the laminar flame F0 is plotted versus HAB for different jet flow speeds. The plot has

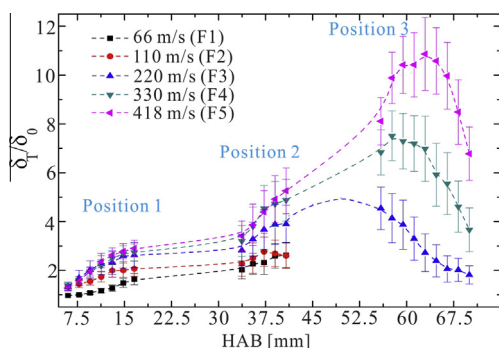


Fig. 5. Thickness of CH layers normalized by the measured laminar CH thickness ($327\text{ }\mu\text{m}$) versus HAB for different jet flow speeds.

been divided into three regions corresponding to the PLIF measurement positions and the error bars represent the standard deviations in CH thickness from 250 samples. Close to the jet exit (Position 1), the thickness increases slightly with axial distance and also gradually increases with flow speed up to 220 m/s . At higher flow speeds, the CH thickness reaches a constant maximum level of $3\delta_0$. At the middle position (Position 2) flames F1 and F2 (i.e. flames in the TRZ regime) approach their tips and do not present a significant broadening; a maximum broadening around $2\delta_0$ could be explained by wrinkled flame fronts and three-dimensional effects. The flame front thickness obtained for flames F1 and F2 at Position 2 is consistent with observations at similar flame conditions previously reported by Sjöholm et al. [17]. In contrast, a continuous increase in CH layer thickness with increasing jet flow speed can be observed for the high Ka flames (F3–F5). This corresponds to the observed CH layer broadening as illustrated in Fig. 2(A2).

At the top position (Position 3), it is obvious that higher flow speed gives larger CH layer thickness. A maximum mean CH thickness of $11\delta_0$, or equivalently 3.6 mm has been observed for flame F5. In flames F3–F5, the CH layer fills up essentially the entire inner part of the flame (regions embraced by the OH radicals, cf. Fig. 2). As the flame tip is approached, the width of the inner region of the flame decreases, which explains the decrease in CH layer thickness at the high flame positions. The observation of CH layer broadening, up to more than 10 times larger than δ_0 , is significant. Reflecting on Driscoll's definition of an experimentally documented distributed reaction zone discussed in the introduction, the existence of distributed reactions induced by turbulence/chemistry interaction, implied for the DRZ regime, is clearly evidenced. If a threshold of $4\delta_0$ were preliminarily set as limit for the DRZ regime, following the discussion in Section 3.1, flame F3 (220 m/s , $Ka=126$) could be assigned to the boundary of the DRZ regime, which is fairly close to $Ka=100$, the boundary of DRZ regime defined by Peters [5].

4. Concluding remarks

The present work focused on characterizing turbulence/flame interactions in the DRZ regime. Simultaneous CH/CH₂O/OH, HCO/CH₂O/OH and T/CH₂O/OH planar imaging measurements have been performed with sufficient spatial resolution for stoichiometric methane/air flames with different flow speeds, covering the laminar flamelet, TRZ and DRZ regimes. The inclusion of HCO in multi-species PLIF measurements was presented for the first time.

A progressive broadening of CH and HCO layers along axial distance has been observed for flames with flow speed above 220 m/s, or Karlovitz number larger than 126. It is demonstrated, for example, in flame F5 (418 m/s, $Ka = 286$, $Re = 40,000$) that broadened or distributed CH and HCO appear from ~ 36 mm HAB and further downstream. The maximum mean CH layer thickness is more than 10 times larger than the laminar CH layer thickness. These observations are, to the best of authors' knowledge, the first experimental verification of a distributed reaction zone.

Observed spatial correlations between different species in the DRZ regime can be summarized as: (1) OH and CH_2O essentially appear mutually exclusive in space; (2) CH (and HCO) can spatially overlap with CH_2O over a large area, and regions of strong CH/HCO signals correspond to relatively weak CH_2O signals and vice versa; (3) CH and HCO are able to penetrate deeper into the OH layer than CH_2O , and overlap with OH signal of medium intensity. The regions where CH and HCO appear distributed show a homogeneous temperature distribution with reduced maximum temperature (~ 1500 K), further supporting the experimental observation of distributed reaction zone.

Acknowledgements

The authors acknowledge financial support from the Swedish Energy Agency (STEM), Swedish Research Council (VR) and the European Research Council (ERC) via Advanced Grant DALDECS.

Appendix A. Supplementary data

Supplementary data associated with this article can be found, in the online version, at <http://dx.doi.org/10.1016/j.proci.2014.06.107>.

References

- [1] N. Peters, *Proc. Combust. Inst.* 21 (1988).
- [2] D. Veynante, J.M. Duclos, J. Piana, *Proc. Combust. Inst.* 25 (1994).
- [3] A. Buschmann, F. Dinkelacker, T. Schafer, et al., *Proc. Combust. Inst.* (1996) 437–445.
- [4] I.G. Shepherd, R.K. Cheng, T. Plessing, et al., *Proc. Combust. Inst.* 29 (2002) 1833–1840.
- [5] N. Peters, *Turbulent Combustion*, Cambridge University Press, Cambridge, 2000.
- [6] Y.C. Chen, M.S. Mansour, *Proc. Combust. Inst.* (1998) 811–818.
- [7] Y.C. Chen, N. Peters, G.A. Schneemann, et al., *Combust. Flame* 107 (1996) 223–244.
- [8] L.P.H. de Goeij, T. Plessing, R.T.E. Hermanns, et al., *Proc. Combust. Inst.* 30 (2005) 859–866.
- [9] M.S. Mansour, N. Peters, Y.C. Chen, *Proc. Combust. Inst.* (1998) 767–773.
- [10] R. Sankaran, E.R. Hawke, J.H. Chen, et al., *Proc. Combust. Inst.* 31 (2007) 1291–1298.
- [11] Z.S. Li, B. Li, Z.W. Sun, et al., *Combust. Flame* 157 (2010) 1087–1096.
- [12] A.Y. Poludnenko, E.S. Oran, *Combust. Flame* 157 (2010) 995–1011.
- [13] W. Meier, X.R. Duan, P. Weigand, *Proc. Combust. Inst.* 30 (2005) 835–842.
- [14] S.Y. Lee, S. Seo, J.C. Broda, et al., *Proc. Combust. Inst.* 28 (2000) 775–782.
- [15] M.J. Dunn, A.R. Masri, R.W. Bilger, et al., *Proc. Combust. Inst.* 32 (2009) 1779–1786.
- [16] J.F. Driscoll, *Prog. Energy Combust.* 34 (2008) 91–134.
- [17] J. Sjöholm, J. Rosell, B. Li, et al., *Proc. Combust. Inst.* 34 (2013) 1475–1482.
- [18] Z.S. Li, J. Kiefer, J. Zetterberg, et al., *Proc. Combust. Inst.* 31 (2007) 727–735.
- [19] B. Zhou, J. Kiefer, J. Zetterberg, et al., *Combust. Flame* 161 (2014) 1566–1574.
- [20] T.W. Lee, A. Mitrovic, *Combust. Sci. Technol.* 127 (1997) 231–249.
- [21] M.J. Dunn, A.R. Masri, R.W. Bilger, *Combust. Flame* 151 (2007) 46–60.
- [22] C. Liu, B. Yan, G. Chen, et al., *Int. J. Hydrogen Energy* 35 (2010) 542–555.
- [23] C. Brackmann, J. Nygren, X. Bai, et al., *Spectrochim. Acta A* 59 (2003) 3347–3356.
- [24] C.M. Vagelopoulos, J.H. Frank, *Proc. Combust. Inst.* 30 (2005) 241–249.
- [25] S.A. Filatyev, J.F. Driscoll, C.D. Carter, et al., *Combust. Flame* 141 (2005) 1–21.
- [26] D. Han, M.G. Mungal, *Combust. Flame* 132 (2003) 565–590.
- [27] H.N. Najm, P.H. Paul, C.J. Mueller, et al., *Combust. Flame* 113 (1998) 312–332.
- [28] B.O. Ayoolan, R. Balachandran, J.H. Frank, et al., *Combust. Flame* 144 (2006) 1–16.
- [29] J.A. Sutton, J.F. Driscoll, *Opt. Lett.* 29 (2004) 2620–2622.
- [30] B. Böhm, J.H. Frank, A. Dreizler, *Proc. Combust. Inst.* 33 (2011) 1583–1590.
- [31] C. Kortschik, T. Plessing, N. Peters, *Combust. Flame* 136 (2004) 43–50.
- [32] T. Plessing, N. Peters, J.G. Wunning, *Proc. Combust. Inst.* (1998) 3197–3204.
- [33] A. Cavaliere, M. de Joannon, *Prog. Energy Combust.* 30 (2004) 329–366.
- [34] I.B. Ozdemir, N. Peters, *Exp. Fluids* 30 (2001) 683–695.